Title

Dihydroceramide desaturase promotes the formation of intraluminal vesicles and inhibits autophagy to increase exosome production

Author List and Affiliations

Chen-Yi Wu[1,2,†], Jhih-Gang Jhang[1,†], Wan-Syuan Lin[1], Chih-Wei Lin[1], Li-An Chu[3,4], Ann-Shyn Chiang[3,5,6,7,8,9], Han-Chen Ho[10], Chih-Chiang Chan[1,*], Shu-Yi Huang[2,*]

[1] Graduate Institute of Physiology, College of Medicine, National Taiwan University, Taipei, Taiwan

[2] Department of Medical Research, National Taiwan University Hospital, Taipei, Taiwan

[3] Brain Research Center, National Tsing Hua University, 101, Section 2, Kuang-Fu Road, Hsinchu 30013, Taiwan

[4] Department of Biomedical Engineering and Environmental Sciences, National Tsing Hua University, 101, Section 2, Kuang-Fu Road, Hsinchu 30013, Taiwan

[5] Institute of Systems Neuroscience, National Tsing Hua University, 101, Section 2, Kuang-Fu Road, Hsinchu 30013, Taiwan

[6] Department of Biomedical Science and Environmental Biology, Kaohsiung Medical University, 100, Shin-Chuan 1st Road, Sanmin Dist., Kaohsiung City 80708, Taiwan

[7] Institute of Molecular and Genomic Medicine, National Health Research Institutes, 35 Keyan Road, Zhunan, Miaoli County 35053, Taiwan

[8] Graduate Institute of Clinical Medical Science, China Medical University, 91, Hsueh-Shih Road, Taichung 40402, Taiwan

[9] Kavli Institute for Brain and Mind, University of California at San Diego, UC San Diego, 9500 Gilman Drive, La Jolla, CA 92093-0115, USA

[10] Department of Anatomy, Tzu Chi University, Hualien, Taiwan

Author List Footnotes

[†] These authors contributed equally to this work.

[*] Lead contacts

Contact Info

Correspondence: shuyih@ntuh.gov.tw and chancc1@ntu.edu.tw

Graphical Abstract

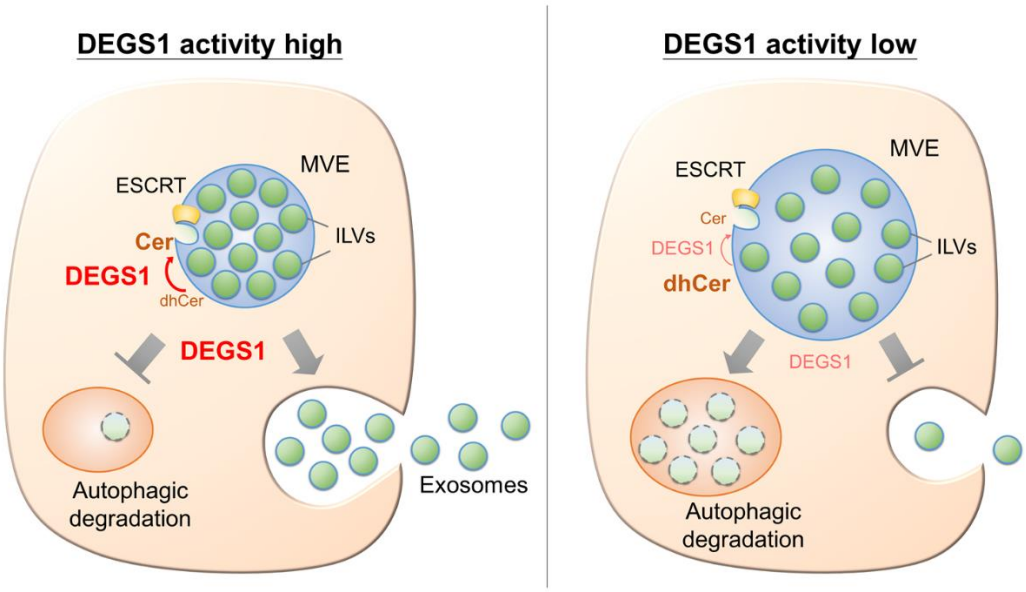

Highlights

- An *in vivo* system was developed for observing exosome production in *Drosophila*.
- Dihydroceramide desaturase (DEGS1/Ifc) promotes exosome production by two means.
- Ifc drives membrane invagination to promote the formation of intraluminal vesicles.
- Ifc inhibits autophagic degradation of MVEs and increases exosome release.

eTOC Blurb

The level and activity of dihydroceramide desaturase (human DEGS1 and Drosophila Ifc) correlate with exosome production. Wu et al. show that DEGS1 drives the formation of intraluminal vesicles *in vivo* and *in vitro*. Overexpressing Ifc inhibits autophagy and reduces the degradation of multivesicular endosomes, thus increases exosome release.

Summary

Exosomes are important for cell-cell communication. Deficiencies in the human dihydroceramide desaturase gene, *DEGS1*, increase the dihydroceramide-to-ceramide ratio and causes hypomyelinating leukodystrophy. However, the disease mechanism remains unknown. Here, we developed an *in vivo* assay with spatially controlled expression of exosome markers in *Drosophila* eye imaginal discs and showed that the level and activity of the DEGS1 ortholog, *ifc*, correlated with exosome production. Knocking out *ifc* decreased the density of the exosome precursor intraluminal vesicles (ILVs) in the multivesicular endosomes and reduced the number of exosomes released. While *ifc* overexpression and autophagy inhibition both enhanced exosome production, combining the two had no additive effect. Moreover, DEGS1 activity was sufficient to drive ILV formation *in vitro*. Together, DEGS1/Ifc controls the dihydroceramide-to-ceramide ration and enhances exosome secretion by promoting ILV formation and preventing the autophagic degradation of MVEs. These findings provide a potential cause for the neuropathy associated with DEGS1-deficient mutations.

Keywords

DEGS1, Ifc, dihydroceramide desaturase, dihydroceramide, ceramide, exosome, autophagy, multivesicular endosome

Introduction

Exosomes are secreted vesicles of approximately 100 nm in diameter that mediate cell-cell communication via the transport of proteins, RNAs, and lipid cargos. In the nervous system, exosomes contribute to the formation and maintenance of myelin sheath (Kramer-Albers et al., 2007). Exosomes originate from the invagination of the endosomal membrane in multivesicular endosomes (MVEs) to form intra-luminal vesicles (ILVs) (Raposo and Stoorvogel, 2013). ILVs can form by a mechanism involving the Endosomal Sorting Complexes Required for Transport (ESCRT) complex, which consists of more than 20 proteins that recruit ubiquitinated protein and other cargos and facilitate the budding and scission of the membrane into the MVE lumen to form ILVs (Katzmann et al., 2001, Adell et al., 2014). ILVs can also form via an ESCRT-independent, ceramide (Cer)-dependent mechanism. Trajkovic et al. (2008) show that the inhibition of neutral sphingomyelinase blocks the conversion of sphingomyelin to Cer and reduces exosome release from oligodendrocytes, suggesting that Cer promotes membrane inward budding for ILV formation. When the MVE membrane fuses with the plasma membrane, ILVs are released to the extracellular space as exosomes. Alternatively, ILV-containing MVEs may be targeted for autophagic-lysosomal degradation. Indeed, inhibition of lysosome-autophagosome fusion by bafilomycin A1 has been shown to increases the secretion of α-synuclein in the exosomes (Poehler et al., 2014, Alvarez-Erviti et al., 2011), suggesting cells may use exosomes as a protective mechanism to remove protein aggregates during lysosomal or autophagic dysfunction. Although a ubiquitin-like post-translational modification called ISGylation has been described to promote MVE degradation and thus block exosome secretion (Villarroya-Beltri et al., 2016), little is known regarding the effect of membrane lipid composition on the fate of MVEs.

The final step of Cer *de novo* synthesis is catalyzed by the enzyme dihydroceramide desaturase (DEGS1 in humans and Ifc in *Drosophila*) which

54 inserts a 4,5-*trans*-double bond into the sphingolipid backbone of
55 dihydroceramide (dhCer) to produce Cer. This structural difference has a
56 profound effect on the biophysical properties of Cer; therefore, the relative
57 abundance of Cer versus dhCer may affect the biological properties of cellular
58 membranes (Li et al., 2002). Indeed, genetic or drug inhibition of DEGS1/Ifc has
59 been shown to cause significant accumulation of dhCer which increases reactive
60 oxygen species, induces autophagy and ER stress, causes cell cycle arrest, and
61 even results in cell death in experimental models (Lee et al., 2012). In humans,
62 variants of the human dhCer desaturase gene, DEGS1, have recently been
63 linked to hypomyelinating leukodystrophy and systemic neuropathy (Dolgin et al.,
64 2019, Karsai et al., 2019, Pant et al., 2019). These reports not only confirm an
65 essential role for DEGS1 in the human nervous system, but also show that loss-
66 of-function mutations of DEGS1cause significant accumulation of dhCer and an
67 overall shift of cellular sphingolipid pool towards the dihydro forms (Karsai et al.,
68 2019). However, the underlying cause of neuropathy associated with loss of
69 DEGS1 activity remains to be investigated.
70
71 Our previous study shows that eye-specific knock-out of Drosophila *ifc*
72 leads to activity-dependent neurodegeneration, supporting a conserved function
73 in the nervous system. We also show that Ifc can function cell non-autonomously,
74 possibly mediated by exosomes (Jung et al., 2017). Although the cellular level of
75 dhCer is low, several studies report the presence of dhCer in the exosome
76 membrane (Brzozowski et al., 2018, Podbielska et al., 2016, Vallabhaneni et al.,
77 2015). Considering ~30% of cellular Cer is estimated to be produced via the *de*
78 *novo* synthesis pathway (Lee et al., 2012), whether DEGS1 activity and dhCer
79 level affect exosome formation and MVE degradation to determine exosome
80 production warrants further study.
81
82 In the present study, we developed an assay to observe exosome
83 secretion *in vivo* by expressing exosome markers in the dorsal half of *Drosophila*
84 eye imaginal discs. This system allowed the quantification of dorsally made

exosomes in response to genetic manipulations on the ventral half of the eye imaginal discs. We also employed the giant unilamellar vesicle (GUV) system to examine if human DEGS1 activity is sufficient to drive the formation of ILVs *in vitro*. Our findings demonstrate an important role for DEGS1/Ifc in regulating both the formation of intraluminal vesicles and the autophagic degradation of MVEs, providing a possible mechanism underlying its function in the nervous system.

Results

Knocking out *ifc* reduces the number of exosomes *in vivo*

To evaluate the role of *ifc* in exosome biogenesis, we established an *in vivo* system with the *Drosophila* eye imaginal discs that have been shown to secret exosomes (Gross et al., 2012). We utilized the Dorsal-Eye Gal4 (*DE-GAL4*) expression system (Morrison and Halder, 2010) to drive the expression of the exosome marker GFP-CD63 (Panakova et al., 2005) restricted to the dorsal half of the disc. We were able to detect the presence of GFP-CD63 puncta in the acellular space above the morphogenetic furrow marked by the lack of DAPI staining on the ventral side of the eye imaginal discs (illustrated in Figure 1A), indicating the movement of GFP-CD63+ extracellular vesicles moving along the dorsal-ventral axis. We collected particles released by the discs and determined their sizes by nanoparticle tracking analysis. The average diameter of the secreted vesicles was 113.8 ± 14.3 nm (Figure 1B), consistent with the size range of exosomes. The morphology of the collected vesicles was also consistent with that of exosomes by transmission electron microscopy (TEM) (Figure 1C). Together, these findings show that the labeled puncta exhibit main characteristics of exosomes based on marker proteins, size distribution, and dorsal-ventral movement (Thery et al., 2018), supporting the use of GFP-CD63 as a surrogate to monitor exosome production in the system of *Drosophila* eye imaginal discs

115 Upon quantification, we found that the number of CD63 puncta detected
116 away from the dorsal compartment was significantly reduced in the *ifc-KO* clones
117 in comparison with the FRT controls (Figures 1D-F). We further utilized this
118 system to express the fusion protein of the flotillin protein Flo2 and RFP as a
119 second exosome marker (Bischoff et al., 2013). Consistent with the results
120 observed with GFP-CD63, *ifc-KO* reduced the number of Flo2-RFP puncta in the
121 ventral compartment (Figure S1). Since *ifc-KO* leads to a drastic accumulation of
122 dhCer, the decrease in exosomes produced by *ifc-KO* clones suggests that the
123 accumulation of dhCer suppresses exosome secretion.
124
125 We then examined the morphology of MVE by analyzing the ultrastructural
126 images of MVEs in wild-type (WT) and *ifc-KO* photoreceptors by TEM. The WT
127 MVEs typically contained densely packed ILVs (Figure 2A). In comparison, the
128 MVEs in *ifc-KO* cells appeared dilated (Figure 2B). Indeed, while the numbers of
129 MVE per view field were similar between WT and mutant photoreceptors (Figure
130 2C, $p = 0.3213$), the size of the MVEs was significantly larger in *ifc-KO*
131 photoreceptors (Figure 2D, $p = 0.0226$). Moreover, the average number of ILVs in
132 each MVE was slightly reduced in *ifc-KO*, although the difference from WT was
133 not statistically significant (Figure 2E, $p = 0.1153$). However, when the size of
134 MVEs was taken into consideration, we found that the density of ILVs was
135 significantly reduced in the mutant MVEs comparing with that of WT (Figure 2F, p
136 < 0.0001). Together, these data show that *ifc-KO* affects the morphology of
137 MVEs.
138
139 <u>Enhancing *ifc* activity increases the number of exosomes</u>
140 To determine whether enhanced *ifc* activity has the opposite effect of *ifc-KO*, we
141 tested the effect of overexpressing wild-type Ifc with a C-terminal mCherry tag
142 (*ifc(WT)-mCherry*) which we have shown to have the ability to rescue the *ifc-KO*
143 phenotype (Jung et al., 2017). Overexpression of *ifc(WT)-mCherry* increased the
144 number of GFP-CD63 puncta comparing with the UAS control of *mCherry-CAAX*
145 overexpression (Figures 3A,B,D). We performed live imaging of *ex vivo* eye

146 imaginal discs using spinning disc confocal microscopy and light-sheet
147 microscopy and found that, in real-time, *ifc(WT)-mCherry* produced more GFP-
148 CD63 puncta than the *mCherry-CAAX* control (Supplemental videos 1-4).
149 Consistently, overexpression of the *ifc(WT)-mCherry* also increased the number
150 of extracellular puncta labeled with another exosome marker TSG101-HA (Thery
151 et al., 2001) (Figure S2). These results suggest that an increased level of Ifc
152 promotes exosome production.
153
154 To investigate whether the catalytic activity of Ifc was required, we mutated
155 one of the highly conserved histidine boxes that are required for the enzyme
156 activity of Ifc (Figure S3A) (Ternes et al., 2002). The mutation did not affect the
157 protein level as we showed by Western blot that the level of Ifc($C3^{mut}$)-mCherry
158 was comparable to that of Ifc(WT)-mCherry (Figures S3B,C). Sphingolipidomics
159 result show that *ifc(C3mut)-mCherry* failed to reverse the increase of dhCer-to-
160 Cer ratio in *ifc-KO*, suggesting that the C3 mutation impaired its catalytic activity
161 (Figure S3D). Overexpression of *ifc($C3^{mut}$)-mCherry* in *ifc-KO* eye imaginal discs
162 failed to increase the number of GFP-CD63 puncta released to the ventral side in
163 comparison with the *mCherry-CAAX* control (Figures 3A,C,D), suggesting that
164 the desaturase activity of Ifc is required to promote the production of exosomes.
165 These results show that the activity of DEGS1/Ifc to convert dhCer to Cer is
166 required to drive exosome formation *in vivo* and demonstrate a correlation
167 between the level and activity of Ifc with exosome production.
168
169 <u>Ifc interacts with ESCRT genes to regulate exosome production</u>
170 Since the role of ESCRT proteins in regulating the process of ILV formation is
171 well studied, we investigated the genetic interactions between *ifc* and the
172 ESCRT-0 gene *hrs* and the ESCRT-II gene *vps25*. Because homozygous
173 mutations of hrs^{D28} and $vps25^{A3}$ are both lethal (Lloyd et al., 2002, Vaccari and
174 Bilder, 2005), we analyzed whether Ifc overexpression genetically interacts with
175 the heterozygous mutations of these two ESCRT genes to regulate exosome
176 production. As expected, the exosomes detected in $hrs^{D28/+}$ and $vps25^{A3/+}$ were

177 significantly fewer than that in wild-type control (Figure S4). We found that
178 overexpression of *ifc(WT)-mCherry* significantly rescued exosome production in
179 *vps25*$^{A3/+}$ but not in *hrs*$^{D28/+}$ (Figure 4). The result indicates that, for exosome
180 formation, overexpression of *ifc* can compensate for the partial loss of *vps25* but
181 not *hrs*. Since ESCRT-0 (Hrs) is important for the recruitment of ubiquitinated
182 cargos while the ESCRT-II (Vps25) complex is necessary for the initiation of
183 membrane invagination and the recruitment of the ESCRT-III complex (Wollert
184 and Hurley, 2010), this finding supports a role for Ifc in the inward budding of
185 MVE membrane during ILV biogenesis but possibly not in cargo recruitment.
186
187 <u>DEGS1 drives the formation of ILVs in GUVs *in vitro*</u>
188 To evaluate if dhCer desaturase is sufficient to drive ILV formation, we resorted to
189 the *in vitro* model membrane system of GUV. After the generation of GUVs, we
190 tracked the morphology of the GUVs over time and observed no spontaneous ILV
191 formation either with or without the inclusion of dhCer in the lipid mixture (Figures
192 5A,B-B',D-D'). Interestingly, when we added human DEGS1 recombinant protein
193 to the GUVs, we were able to observe the formation of ILVs in the GUVs that
194 contained dhCer within 5 minutes (Figures 5A,C-C',E-E'). When we added the
195 DEGS1 inhibitor fenretinide to the system, the formation of ILVs by DEGS1 was
196 blocked (Figures 5F,J-J'); the ethanol solvent control had no such inhibitory effect
197 (Figures 5F,H-H'). Therefore, the activity of DEGS1 was sufficient to drive the
198 formation of ILV *in vitro* by converting dhCer to Cer. These data further support
199 that the catalytic activity of DEGS1 promotes membrane invagination for the
200 initiation of exosome biogenesis.
201
202 <u>Ifc promotes exosome secretion by blocking autophagy-mediated degradation of</u>
203 <u>MVEs</u>
204 We and others have reported autophagy induction as a common outcome of
205 *DEGS1/ifc* inhibition not only in *Drosophila* but also in mammalian cell lines and
206 animal models (Barbarroja et al., 2015, Holland et al., 2007, Jung et al., 2017,
207 Kraveka et al., 2007). In addition, we previously identified the endosomal

208 localization of Ifc (Jung et al., 2017) and herein showed the regulation of
209 DEGS1/Ifc in exosome secretion. Therefore, we hypothesized that DEGS1/Ifc
210 functions as the pivot of MVB fate between autophagic degradation versus fusion
211 with the plasma membrane for exosome release. To evaluate the interrelationship
212 between autophagy and exosome pathways, we inhibited autophagy by feeding
213 the *Drosophila* larvae 3-methyladenine (3-MA) and chloroquine to block the
214 formation of autophagosome and prevent autophagosomes-lysosome fusion,
215 respectively (Tang et al., 2017, Jung et al., 2017). Inhibition of autophagy by 3-
216 MA and chloroquine both increased the numbers of GFP-CD63+ vesicles
217 released in the wild-type background (Figures 6A-D). Consistent with the results
218 shown in Figure 3, over-expression of *ifc(WT)-mCherry* increased the number of
219 ELVs (Figures 6A,E). Interestingly, feeding 3-MA or chloroquine to larvae
220 overexpressing *ifc* did not further increase the number of GFP-CD63 exosomes
221 in the ventral morphogenetic furrow (Figures 6E-H). These data suggest that
222 GFP-CD63 puncta in MVEs underwent autophagy-mediated degradation in *ifc-*
223 *KO* and suggest that Ifc promotes the production of exosomes by inhibiting
224 autophagy.
225
226

227 # Discussion

228 In the present study, we developed an *in vivo* system for the analysis of exosome
229 production using *Drosophila* eye imaginal discs with the dorsal expression of
230 GFP-CD63. The validity of the system was supported by two additional exosome
231 markers, Flo2 and Tsg101, as well as size measurement by nanoparticle tracking
232 analysis. We showed *in vivo* and *in vitro* that the release of exosomes from the
233 dorsal half of *Drosophila* eye imaginal discs to the ventral morphogenetic furrow
234 correlated with not only the level but also the activity of the dihydroceramide
235 desaturase, *ifc*. Our genetic analysis and GUV assay support a clear role for Ifc
236 in the early stage of ILV formation in promoting membrane invagination. In
237 addition, *ifc* also affects the degradation of MVEs via autophagy. Overexpression

238 of *ifc* inhibits autophagy to preserve MVEs thus increase exosome secretion.
239 Together, our data show that DEGS1/Ifc promotes membrane invagination of ILV
240 formation during exosome biogenesis and prevents the autophagic degradation
241 of MVEs, thus promoting exosome formation and release.
242
243 Between the ESCRT-dependent and Cer-mediated mechanisms of
244 exosome biogenesis, it is generally believed that the ESCRT-dependent
245 mechanism is involved in the selective sorting of cargos, whereas the Cer-
246 dependent mechanisms are important to control the initial membrane budding
247 (Larios et al., 2020, Teis et al., 2010, Trajkovic et al., 2008). Here, we found that
248 overexpression of *ifc(WT)-mCherry* could rescue the exosome numbers in the
249 heterozygous mutant of *vps25* but not in that of *hrs*, suggesting that *ifc* does not
250 regulate cargo loading. However, *Kajimoto et al. (2013)* show that the continuous
251 Cer catabolism produces sphingosine 1-phosphate that is required for cargo
252 sorting into ILVs in human cells. Exosome membranes share similar lipid
253 composition with lipid rafts, both highly enriched for cholesterol and sphingolipids
254 (Hebbar et al., 2008). Lipid rafts are rigid membrane microdomains that serve as
255 a platform for protein-protein interaction and are essential for protein activation
256 and signal transduction (Lingwood and Simons, 2010). Cer-rich domains have
257 been recognized to affect raft properties by competing and displacing cholesterol
258 (Megha and London, 2004) and promoting the formation of highly ordered gel
259 phases (Bieberich, 2018). The Cer-rich membrane domains may not only serve
260 as a permissive environment to promote membrane invagination for ILV
261 formation, but may also behave as a platform to facilitate the recruitment of
262 ESCRT components. We have previously reported that Ifc predominantly resides
263 in the endosomes in *Drosophila* photoreceptors (Jung et al., 2017), which
264 suggests an on-site conversion of dhCer into Cer for the dynamic regulation of
265 membrane property. How the levels of Cer vs. dhCer on local membranes
266 influence biological processes such as ILV formation need to be further
267 investigated.
268

269 Several previous studies have shown that inhibition of autophagosome-
270 lysosome degradation enhances exosome secretion (Danzer et al., 2012, Fader
271 et al., 2008, Iguchi et al., 2016). Interestingly, inhibition of autophagy by
272 Bafilomycin A1 (BafA1) not only increases the secretion of CD63+ exosomes but
273 also increases the detection of autophagic proteins p62 and LC3 in exosomes
274 (Minakaki et al., 2018). However, autophagy proteins ATG12–ATG3 have been
275 shown to interact with the ESCRT-associated protein Alix to promote late
276 endosome to lysosome trafficking as well as exosome biogenesis (Murrow et al.,
277 2015). Also, knockout of ATG5 but not ATG7 significantly reduces the number of
278 exosomes, suggesting that not all of the autophagy core components participate
279 in the regulation of exosome release (Guo et al., 2017). In addition, exosomes
280 purified from cultured cortical neurons treated with BafA1 show a ~2-fold
281 increase in certain sphingolipid species, including Cer and dhCer, indicating
282 BafA1 affects the lipid composition of exosomes (Miranda et al., 2018). Leidal et
283 al. (2020) report that LC3 and LC3-conjugation machinery recruit specific cargos
284 to pack into LC3-positive EVs for secretion, a process that does not require the
285 ESCRT complex but is dependent on the activity of neutral sphingomyelinase 2,
286 an enzyme that hydrolyzes sphingomyelin to produced Cer. In the present study,
287 we showed that exosome production increased with the inhibition of autophagy
288 by either 3-MA or chloroquine. However, combining autophagy inhibition and *ifc*
289 overexpression did not further increase exosome production, implying that *ifc*
290 overexpression inhibits autophagy in opposite to *ifc-KO* which induces
291 autophagy. Membrane Cer/dhCer may play an important role in controlling the
292 fate of MVEs between autophagic degradation and secretion of exosomes;
293 further study is warranted to elucidate the mechanism in detail.
294
295 While the effects of Cer have been extensively studied in various contexts,
296 our findings draw attention to dhCer, which is a long-ignored sphingolipid
297 species. Although dhCer is structurally different from Cer only in the lack of the
298 4,5-double bond, the two sphingolipid species have widely different biophysical
299 properties and bioactivities. Several previous studies have hinted at a role for

dhCer in the nervous system. Jung et al. (2017) show that eye-specific *ifc-KO* results in activity-dependent neurodegeneration and demonstrated that *ifc* can function cell non-autonomously. Inherited DEGS1 deficiencies lead to hypomyelination in the central and peripheral nervous systems (Dolgin et al., 2019, Karsai et al., 2019, Pant et al., 2019). Since exosomes are important for myelination and demyelination, whether altered exosome production is the underlying cause of defects seen in patients with inherited DEGS1 deficiencies warrants further investigation.

Materials and Methods

Key Resources Table

REAGENT or RESOURCE	SOURCE	IDENTIFIER
Antibodies		
Mouse anti-CD63	Developmental Studies Hybridoma Bank (DSHB)	Cat# H5C6; RRID: AB_528158
DAPI	ThermoFisher	Cat# D1306; RRID: AB_2629482
Anti-RFP	Rockland	Cat# 600-401-379; RRID: AB_2209751
Anti-HA	Cell Signaling Technology	Cat# 3724; RRID: AB_1549585
Anti-mCherry	GeneTex	Cat# GTX630189
Anti-Actin	Millipore	Cat# MAB1501; RRID: AB_2223041
anti-mouse-HRP	Jackson ImmunoResearch Laboratories, Inc.	Cat# 115-005-003; RRID: AB_2338447
***Drosophila* Strains**		
ey-FLP	Bloomington stock center (BDSC)	5622

cl, FRT40A		5622
FRT40A		5615
DE-Gal4		29650
UAS-mCherry-CAAX		59021
UAS-hTSG101-HA		77977
hrs^{D28}		54574
vps25^{A3}		39633
ifc-KO, FRT40A	Jung et al. (2017)	
UAS-*ifc(WT)*-mCherry		
UAS-EGFP-CD63	Gift from Dr. Suzanne Eaton (Panakova et al., 2005)	
UAS-*ifc(C3*^{mut}*)*-mCherry	This study	
UAS-Flo2-RFP	Bischoff et al. (2013)	
Chemicals and other reagents		
Recombinant human DEGS1 protein	Abcam	ab160100
Sucrose	Sigma	S7903
NaCl		31434
Glucose		G8270
NADPH		1010782400
ATP		A2383
$MgCl_2$	Calbiochem	442611

Experimental Model and Subject Details

Drosophila strains and genetics

Drosophila stocks were maintained at 25°C on standard medium and genetic crosses were performed following standard fly husbandry procedures. Information on individual fly strains can be found on FlyBase (flybase.org) unless otherwise noted in the above Key Resources Table.

Immunohistochemistry and confocal microscopy

For immunofluorescence staining, larval eye imaginal discs were dissected, fixed,

323 washed, and immunostained with primary and secondary antibodies as
324 previously described (Jung et al., 2017). The antibodies used were listed in the
325 above Key Resources Table. All samples were mounted in Vectashield (Vector
326 Laboratories) and analyzed on a Carl Zeiss LSM880 confocal microscope with
327 LAS AF software. Imaging data were processed and quantified using Photoshop
328 (CS6; Adobe), Illustrator (CS6; Adobe), and ImageJ (National Institutes of
329 Health).
330
331 **Nanoparticle tracking analysis**
332 Fifty to 100 eye imaginal discs were dissected and incubated in sterile-filtered
333 Schneider medium (Gibco 21720024) with low-speed agitation (7 rpm) at room
334 temperature for 2.5 h. The supernatant was then separated by low-speed
335 centrifugation at 3,000 x g for 15 min to remove large debris, followed by another
336 centrifugation at 12,000 x g for 15 min. The samples were then passed through a
337 Smart SEC single column (System Biosciences, USA) for EV isolation. The size
338 distribution was determined using NanoSight NS300 (Malvern Panalytical Ltd,
339 United Kingdom) under constant flow (flow rate = 70) at 25°C. The recordings
340 were analyzed by NTA 3.4 software Build 3.4.003 with the detection threshold set
341 to 6.
342
343 **Transmission electron microscopy and image analysis of MVE morphology**
344 Exosome samples were prepared as described for nanoparticle tracking analysis.
345 Transmission electron microscopy was performed as previously described (Jung
346 et al., 2017). To characterize the MVE morphology, the fields of imaging for the
347 characterization within the eye of each genotype were selected randomly, and
348 the image files were blinded for the analyses of both the area of MVE and the
349 number of ILV. The area and number of MVE were quantified using Photoshop.
350
351 **Timelapse live imaging of exosome secretion**
352 For live imaging of exosome secretion by spinning disc confocal microscopy,
353 timelapse images were aquired using a Zeiss spinning disc microscope equipped

354 with a Yokogawa CSU-X1 scanner unit and a high-resolution CCD (Phtometrics
355 PRISM 95B). Images were acquired through a 40X objective with an exposure
356 time of 200 ms every 5 minutes for 80 min. For live imaging of exosome secretion
357 by light sheet microscopy, the Gaussian intensity distribution of the laser was
358 projecting to an annular ring pattern on the customized aluminum coating mask
359 (thickness of 1,500 angstroms). The masked laser ring image was then projected
360 to a set of galvanometer scanners (6215H, Cambridge Technology) which were
361 composed of a pair of achromatic lenses (Thorlabs, AC254-100-A, Achromat,
362 Ø1", 400–750 nm), aligned in a 4f arrangement. After passing through the
363 scanning mirror set, the ring pattern was magnified through a relay lens
364 (Thorlabs, AC254-250-A and AC254-350-A Ø1" Achromat, 400–750 nm) and
365 conjugated to the back focal plane of the excitation objective (Nikon CFI Plan
366 Fluorite Objective, 0.30 NA, 3.5 mm WD). The annular pattern was projected to
367 the rear focal plane of the excitation objective and forms a self-reconstructive
368 Bessel beam by optical interference. The signal was detected by a 25X and an
369 sCMOS camera (Hamamatsu, Orca Flash 4.0 v3 sCMOS). Thirty frames were
370 acquired at each time point, with the exposure time of 30 ms for an area of 300
371 μm x 300 μm. The images for each time point were converted into 4D time series
372 by Imaris 9.1.1. (Bitplane AG).
373
374 **Site-directed mutagenesis of *UAS-ifc* mutants**
375 To generate point mutations in the catalytic domain of *UAS-ifc* transgene, the
376 pUASt-ifc was used as a backbone and site-directed mutagenesis was done with
377 QuikChange Kit (Agilent 200523) following the manufacturer's instruction. All
378 constructs were verified by sequencing. Transgenic flies were generated by
379 embryo injection according to standard protocols of integrase-mediated insertion
380 (Bischof et al., 2007) followed by a germline transmission screen. Primer
381 sequences for *ifc(C3^{mut})* were: (FWD) GCCAACGAGGCCGCCGACTTTCCG;
382 (REV) GGCGGCCTCGTTGGCGTAGCCCAC.
383
384 **Western blotting**

385 The protein extracts were prepared with dissected fly tissues that were
386 homogenized for 10 min at 4°C in 1x RIPA buffer containing protease inhibitors
387 (ThermoFisher A32955), followed by centrifugation at 16,000 x g for 15min at 4°C
388 to remove the debris. The supernatant of the homogenates was mixed with 4X
389 sample buffer (20% glycerol, 4% SDS, 100 mM Tris pH 6.8, 0.002%
390 Bromophenol blue), boiled for 10 min, separated by SDS-PAGE, and transferred
391 in a wet-transfer tank to PVDF membranes (Millipore, IPVH00010) following
392 manufacturer's instructions (Bio-Rad). PVDF membranes were incubated with
393 5% non-fat milk in TBST [10 mM Tris (pH 8.0), 150 mM NaCl, 0.1% Tween 20] for
394 1 h at room temperature and then incubated with primary antibodies at 4°C
395 overnight. Membranes were then washed three times with TBST for 10 min each
396 before incubating with secondary antibodies in TBST for 1 h at room
397 temperature, washed with TBST three times, and developed with ECL reagents
398 (Millipore, WBKLS0500). The signals were captured by the BioSpectrum™ 600
399 Imaging System (UVP Ltd), and the relative intensities of bands were quantified
400 by densitometry using the Image J software (Schneider et al., 2012).
401
402 **Sphingolipidomics**
403 Sphingolipid extraction was performed as described {Jung, 2017 #57}. Briefly,
404 500 larvae (male and female were equally represented) were snap-frozen in
405 liquid nitrogen and homogenized by grinding.
406
407 **Giant Unilamellar Vesicle (GUV) assay**
408 GUV was prepared by the electroformation method (Lee et al., 2018). Briefly, the
409 lipid mixture of Dioleoylphosphatidylcholine (DOPC) and cholesterol was
410 dissolved in chloroform at 1:0.67 molar ratio to the final concentration of 15mM.
411 For lipid mixture with dhCer, the lipid mixture included DOPC:dhCer:cholesterol
412 at 1:1:0.67 molar ratio to the total concentration of 15mM. The lipid mixture was
413 then deposited into a chamber made with a rubber O-ring on an electrically
414 conductive ITO glass. The setup was vacuum dried at 50°C for 1 h, and the
415 solvent was evaporated thereby producing a thin lipid film. The chamber was

then re-filled with 2ml of 400mM sucrose. Depending on the experimental conditions, 0.2 μM of the DEGS1 inhibitor fenretinide might be added to the sucrose solution. After sealing the chamber with another piece of ITO glass, the setup was supplied with a sinusoidal voltage waveform of 3.5 V amplitude at 10 Hz frequency and kept at 65°C overnight. The unilamellar vesicles were cooled down and resuspended in 200 μl of 400mM glucose, and confocal images were acquired using Zeiss Cell Observer SD to show the morphology of GUV at time = 0. The recombinant DEGS1 protein at the concentration of 9.62 nM and co-factors (ATP 4 mM, NADPH 2 mM, MgCl2 2.4 mM, NaCl 50 mM, and sucrose 50 mM) were then supplemented to the GUV/sucrose mixture. The post-treatment images were acquired after 5 min of incubation at 37°C.

Quantification and statistical analysis

Quantitative data were analyzed using a two-tailed unpaired Student's *t*-test or one-way ANOVA with Tukey's multiple comparison test. Data analysis was performed using GraphPad Prism 5. All data in bar graphs are shown as mean ± SEM. The quantified GFP-CD63 puncta in the experimental groups were normalized to the average of the controls which was set as 1. *P* values of less than 0.05 were regarded as statistically significant. All quantifications included at least three experimental replicates.

Acknowledgments

The authors are grateful to Drs. Guang-Chao Chen, Robin Hiesinger, Jennifer Jin, Guang Lin, Ya-Wen Liu, Yi Henry Sun, Chao-Wen Wang, Chi-Kuang Yao, and Mr. Fei-Yang Tzou for their comments on the manuscript. The authors sincerely thank Dr. Ya-Wen Liu and Ms. Yu-Chen Chang for helping us established the GUV system. We thank the staff of the Imaging Core at the First Core Lab, National Taiwan University College of Medicine, the Second Core Lab, Department of Medical Research, National Taiwan University Hospital, and the

Electron Microscopy Laboratory, Tzu Chi University, for technical support. We thank WellGenetics, Inc. for embryo injection service. Stocks obtained from the Bloomington Drosophila Stock Center (NIH P40OD018537) were used in this study. This work was supported by the Ministry of Science and Technology of Taiwan grants 107-2635-B-002-001 to S.-Y. Huang and 108-2311-B-002-011-MY3 to C.-C. Chan, National Taiwan University Hospital grant 109-21 to S.-Y. Huang, and National Taiwan University grant 109L104308 to C.-C. Chan.

Author contributions

S.-Y. Huang and C.-C. Chan conceived the study; C.-Y. Wu, J.-G. Jhang, W.-S. Lin, and C.-W. Lin carried out the fly experiments; J.-G. Jhang developed the *in vivo* exosome release assay; C.-Y. Wu and H.-C. Ho carried out the EM analysis; C.-Y. Wu, L.-A. Chu, and A.-S. Chiang performed live imaging; C.-Y. Wu designed and carried out the GUV experiments; C.-Y. Wu, W.-S. Lin, and S.-Y. Huang prepared the figures; S.-Y. Huang wrote the first draft; S.-Y. Huang, and C.-C. Chan reviewed and edited the manuscript with comments from all other authors; S.-Y. Huang and C.-C. Chan obtained the funding for the project; S.-Y. Huang and C.-C. Chan supervised the project.

Declaration of interests

The authors declare no competing interests.

Abbreviations

Cer, ceramide;
dhCer, dihydroceramide;
ESCRT, Endosomal Sorting Complexes Required for Transport;
GUV, giant unilamellar vesicles;
ILVs, intraluminal vesicles;

474 MVEs, multivesicular endosomes.

References

Adell, M. A., Vogel, G. F., Pakdel, M., Muller, M., Lindner, H., Hess, M. W. & Teis, D. 2014. Coordinated binding of Vps4 to ESCRT-III drives membrane neck constriction during MVB vesicle formation. *J Cell Biol,* 205**,** 33-49. DOI: https://doi.org/10.1083/jcb.201310114.

Alvarez-Erviti, L., Seow, Y., Schapira, A. H., Gardiner, C., Sargent, I. L., Wood, M. J. & Cooper, J. M. 2011. Lysosomal dysfunction increases exosome-mediated alpha-synuclein release and transmission. *Neurobiol Dis,* 42**,** 360-7. DOI: https://doi.org/10.1016/j.nbd.2011.01.029.

Barbarroja, N., Rodriguez-Cuenca, S., Nygren, H., Camargo, A., Pirraco, A., Relat, J., Cuadrado, I., Pellegrinelli, V., Medina-Gomez, G., Lopez-Pedrera, C., Tinahones, F. J., Symons, J. D., Summers, S. A., Oresic, M. & Vidal-Puig, A. 2015. Increased dihydroceramide/ceramide ratio mediated by defective expression of degs1 impairs adipocyte differentiation and function. *Diabetes,* 64**,** 1180-92. DOI: https://doi.org/10.2337/db14-0359.

Bieberich, E. 2018. Sphingolipids and lipid rafts: Novel concepts and methods of analysis. *Chem Phys Lipids,* 216**,** 114-131. DOI: https://doi.org/10.1016/j.chemphyslip.2018.08.003.

Bischof, J., Maeda, R. K., Hediger, M., Karch, F. & Basler, K. 2007. An optimized transgenesis system for Drosophila using germ-line-specific phiC31 integrases. *Proc Natl Acad Sci U S A,* 104**,** 3312-7. DOI: https://doi.org/10.1073/pnas.0611511104.

Bischoff, M., Gradilla, A. C., Seijo, I., Andres, G., Rodriguez-Navas, C., Gonzalez-Mendez, L. & Guerrero, I. 2013. Cytonemes are required for the establishment of a normal Hedgehog morphogen gradient in Drosophila epithelia. *Nat Cell Biol,* 15**,** 1269-81. DOI: https://doi.org/10.1038/ncb2856.

Brzozowski, J. S., Jankowski, H., Bond, D. R., Mccague, S. B., Munro, B. R., Predebon, M. J., Scarlett, C. J., Skelding, K. A. & Weidenhofer, J. 2018. Lipidomic profiling of extracellular vesicles derived from prostate and prostate cancer cell lines. *Lipids Health Dis,* 17**,** 211. DOI: https://doi.org/10.1186/s12944-018-0854-x.

Danzer, K. M., Kranich, L. R., Ruf, W. P., Cagsal-Getkin, O., Winslow, A. R., Zhu, L., Vanderburg, C. R. & Mclean, P. J. 2012. Exosomal cell-to-cell transmission of alpha synuclein oligomers. *Mol Neurodegener,* 7**,** 42. DOI: https://doi.org/10.1186/1750-1326-7-42.

Dolgin, V., Straussberg, R., Xu, R., Mileva, I., Yogev, Y., Khoury, R., Konen, O., Barhum, Y., Zvulunov, A., Mao, C. & Birk, O. S. 2019. DEGS1 variant causes neurological disorder. *Eur J Hum Genet,* 27**,** 1668-1676. DOI: https://doi.org/10.1038/s41431-019-0444-z.

Fader, C. M., Sanchez, D., Furlan, M. & Colombo, M. I. 2008. Induction of autophagy promotes fusion of multivesicular bodies with autophagic vacuoles in k562 cells. *Traffic,* 9**,** 230-50. DOI: https://doi.org/10.1111/j.1600-0854.2007.00677.x.

Gross, J. C., Chaudhary, V., Bartscherer, K. & Boutros, M. 2012. Active Wnt proteins are secreted on exosomes. *Nat Cell Biol,* 14**,** 1036-45. DOI:

517 https://doi.org/10.1038/ncb2574.
518 Guo, H., Chitiprolu, M., Roncevic, L., Javalet, C., Hemming, F. J., Trung, M. T., Meng, L.,
519 Latreille, E., Tanese De Souza, C., Mcculloch, D., Baldwin, R. M., Auer, R., Cote, J.,
520 Russell, R. C., Sadoul, R. & Gibbings, D. 2017. Atg5 Disassociates the V1V0-ATPase
521 to Promote Exosome Production and Tumor Metastasis Independent of Canonical
522 Macroautophagy. *Dev Cell,* 43**,** 716-730 e7. DOI:
523 https://doi.org/10.1016/j.devcel.2017.11.018.
524 Hebbar, S., Lee, E., Manna, M., Steinert, S., Kumar, G. S., Wenk, M., Wohland, T. & Kraut,
525 R. 2008. A fluorescent sphingolipid binding domain peptide probe interacts with
526 sphingolipids and cholesterol-dependent raft domains. *J Lipid Res,* 49**,** 1077-89.
527 DOI: https://doi.org/10.1194/jlr.M700543-JLR200.
528 Holland, W. L., Brozinick, J. T., Wang, L. P., Hawkins, E. D., Sargent, K. M., Liu, Y., Narra, K.,
529 Hoehn, K. L., Knotts, T. A., Siesky, A., Nelson, D. H., Karathanasis, S. K., Fontenot, G.
530 K., Birnbaum, M. J. & Summers, S. A. 2007. Inhibition of ceramide synthesis
531 ameliorates glucocorticoid-, saturated-fat-, and obesity-induced insulin resistance.
532 *Cell Metab,* 5**,** 167-79. DOI: https://doi.org/10.1016/j.cmet.2007.01.002.
533 Iguchi, Y., Eid, L., Parent, M., Soucy, G., Bareil, C., Riku, Y., Kawai, K., Takagi, S., Yoshida, M.,
534 Katsuno, M., Sobue, G. & Julien, J. P. 2016. Exosome secretion is a key pathway for
535 clearance of pathological TDP-43. *Brain,* 139**,** 3187-3201. DOI:
536 https://doi.org/10.1093/brain/aww237.
537 Jung, W. H., Liu, C. C., Yu, Y. L., Chang, Y. C., Lien, W. Y., Chao, H. C., Huang, S. Y., Kuo, C. H.,
538 Ho, H. C. & Chan, C. C. 2017. Lipophagy prevents activity-dependent
539 neurodegeneration due to dihydroceramide accumulation in vivo. *EMBO Rep,* 18**,**
540 1150-1165. DOI: https://doi.org/10.15252/embr.201643480.
541 Kajimoto, T., Okada, T., Miya, S., Zhang, L. & Nakamura, S. 2013. Ongoing activation of
542 sphingosine 1-phosphate receptors mediates maturation of exosomal
543 multivesicular endosomes. *Nat Commun,* 4**,** 2712. DOI:
544 https://doi.org/10.1038/ncomms3712.
545 Karsai, G., Kraft, F., Haag, N., Korenke, G. C., Hanisch, B., Othman, A., Suriyanarayanan, S.,
546 Steiner, R., Knopp, C., Mull, M., Bergmann, M., Schroder, J. M., Weis, J., Elbracht,
547 M., Begemann, M., Hornemann, T. & Kurth, I. 2019. DEGS1-associated aberrant
548 sphingolipid metabolism impairs nervous system function in humans. *J Clin Invest,*
549 129**,** 1229-1239. DOI: https://doi.org/10.1172/JCI124159.
550 Katzmann, D. J., Babst, M. & Emr, S. D. 2001. Ubiquitin-dependent sorting into the
551 multivesicular body pathway requires the function of a conserved endosomal
552 protein sorting complex, ESCRT-I. *Cell,* 106**,** 145-55. DOI:
553 https://doi.org/10.1016/s0092-8674(01)00434-2.
554 Kramer-Albers, E. M., Bretz, N., Tenzer, S., Winterstein, C., Mobius, W., Berger, H., Nave, K.
555 A., Schild, H. & Trotter, J. 2007. Oligodendrocytes secrete exosomes containing
556 major myelin and stress-protective proteins: Trophic support for axons?
557 *Proteomics Clin Appl,* 1**,** 1446-61. DOI: https://doi.org/10.1002/prca.200700522.
558 Kraveka, J. M., Li, L., Szulc, Z. M., Bielawski, J., Ogretmen, B., Hannun, Y. A., Obeid, L. M. &
559 Bielawska, A. 2007. Involvement of dihydroceramide desaturase in cell cycle
560 progression in human neuroblastoma cells. *J Biol Chem,* 282**,** 16718-28. DOI:

561 https://doi.org/10.1074/jbc.M700647200.
562 Larios, J., Mercier, V., Roux, A. & Gruenberg, J. 2020. ALIX- and ESCRT-III-dependent sorting
563 of tetraspanins to exosomes. *J Cell Biol,* 219. DOI:
564 https://doi.org/10.1083/jcb.201904113.
565 Lee, C. W., Chiang, Y. L., Liu, J. T., Chen, Y. X., Lee, C. H., Chen, Y. L. & Hwang, I. S. 2018.
566 Emerging Roles of Air Gases in Lipid Bilayers. *Small,* 14**,** e1802133. DOI:
567 https://doi.org/10.1002/smll.201802133.
568 Lee, S. Y., Kim, J. R., Hu, Y., Khan, R., Kim, S. J., Bharadwaj, K. G., Davidson, M. M., Choi, C.
569 S., Shin, K. O., Lee, Y. M., Park, W. J., Park, I. S., Jiang, X. C., Goldberg, I. J. & Park, T.
570 S. 2012. Cardiomyocyte specific deficiency of serine palmitoyltransferase subunit
571 2 reduces ceramide but leads to cardiac dysfunction. *J Biol Chem,* 287**,** 18429-39.
572 DOI: https://doi.org/10.1074/jbc.M111.296947.
573 Leidal, A. M., Huang, H. H., Marsh, T., Solvik, T., Zhang, D., Ye, J., Kai, F., Goldsmith, J., Liu,
574 J. Y., Huang, Y. H., Monkkonen, T., Vlahakis, A., Huang, E. J., Goodarzi, H., Yu, L.,
575 Wiita, A. P. & Debnath, J. 2020. The LC3-conjugation machinery specifies the
576 loading of RNA-binding proteins into extracellular vesicles. *Nat Cell Biol,* 22**,** 187-
577 199. DOI: https://doi.org/10.1038/s41556-019-0450-y.
578 Li, L., Tang, X., Taylor, K. G., Dupre, D. B. & Yappert, M. C. 2002. Conformational
579 characterization of ceramides by nuclear magnetic resonance spectroscopy.
580 *Biophys J,* 82**,** 2067-80. DOI: https://doi.org/10.1016/S0006-3495(02)75554-9.
581 Lingwood, D. & Simons, K. 2010. Lipid rafts as a membrane-organizing principle. *Science,*
582 327**,** 46-50. DOI: https://doi.org/10.1126/science.1174621.
583 Lloyd, T. E., Atkinson, R., Wu, M. N., Zhou, Y., Pennetta, G. & Bellen, H. J. 2002. Hrs regulates
584 endosome membrane invagination and tyrosine kinase receptor signaling in
585 Drosophila. *Cell,* 108**,** 261-9. DOI: https://doi.org/10.1016/s0092-
586 8674(02)00611-6.
587 Megha & London, E. 2004. Ceramide selectively displaces cholesterol from ordered lipid
588 domains (rafts): implications for lipid raft structure and function. *J Biol Chem,* 279**,**
589 9997-10004. DOI: https://doi.org/10.1074/jbc.M309992200.
590 Minakaki, G., Menges, S., Kittel, A., Emmanouilidou, E., Schaeffner, I., Barkovits, K.,
591 Bergmann, A., Rockenstein, E., Adame, A., Marxreiter, F., Mollenhauer, B., Galasko,
592 D., Buzas, E. I., Schlotzer-Schrehardt, U., Marcus, K., Xiang, W., Lie, D. C., Vekrellis,
593 K., Masliah, E., Winkler, J. & Klucken, J. 2018. Autophagy inhibition promotes
594 SNCA/alpha-synuclein release and transfer via extracellular vesicles with a hybrid
595 autophagosome-exosome-like phenotype. *Autophagy,* 14**,** 98-119. DOI:
596 https://doi.org/10.1080/15548627.2017.1395992.
597 Miranda, A. M., Lasiecka, Z. M., Xu, Y., Neufeld, J., Shahriar, S., Simoes, S., Chan, R. B.,
598 Oliveira, T. G., Small, S. A. & Di Paolo, G. 2018. Neuronal lysosomal dysfunction
599 releases exosomes harboring APP C-terminal fragments and unique lipid
600 signatures. *Nat Commun,* 9**,** 291. DOI: https://doi.org/10.1038/s41467-017-
601 02533-w.
602 Morrison, C. M. & Halder, G. 2010. Characterization of a dorsal-eye Gal4 Line in Drosophila.
603 *Genesis,* 48**,** 3-7. DOI: https://doi.org/10.1002/dvg.20571.
604 Murrow, L., Malhotra, R. & Debnath, J. 2015. ATG12-ATG3 interacts with Alix to promote

605 basal autophagic flux and late endosome function. *Nat Cell Biol,* 17**,** 300-10. DOI:
606 https://doi.org/10.1038/ncb3112.
607 Panakova, D., Sprong, H., Marois, E., Thiele, C. & Eaton, S. 2005. Lipoprotein particles are
608 required for Hedgehog and Wingless signalling. *Nature,* 435**,** 58-65. DOI:
609 https://doi.org/10.1038/nature03504.
610 Pant, D. C., Dorboz, I., Schluter, A., Fourcade, S., Launay, N., Joya, J., Aguilera-Albesa, S.,
611 Yoldi, M. E., Casasnovas, C., Willis, M. J., Ruiz, M., Ville, D., Lesca, G., Siquier-Pernet,
612 K., Desguerre, I., Yan, H., Wang, J., Burmeister, M., Brady, L., Tarnopolsky, M.,
613 Cornet, C., Rubbini, D., Terriente, J., James, K. N., Musaev, D., Zaki, M. S., Patterson,
614 M. C., Lanpher, B. C., Klee, E. W., Pinto, E. V. F., Wohler, E., Sobreira, N. L. M., Cohen,
615 J. S., Maroofian, R., Galehdari, H., Mazaheri, N., Shariati, G., Colleaux, L., Rodriguez,
616 D., Gleeson, J. G., Pujades, C., Fatemi, A., Boespflug-Tanguy, O. & Pujol, A. 2019.
617 Loss of the sphingolipid desaturase DEGS1 causes hypomyelinating leukodystrophy.
618 *J Clin Invest,* 129**,** 1240-1256. DOI: https://doi.org/10.1172/JCI123959.
619 Podbielska, M., Szulc, Z. M., Kurowska, E., Hogan, E. L., Bielawski, J., Bielawska, A. & Bhat,
620 N. R. 2016. Cytokine-induced release of ceramide-enriched exosomes as a
621 mediator of cell death signaling in an oligodendroglioma cell line. *J Lipid Res,* 57**,**
622 2028-2039. DOI: https://doi.org/10.1194/jlr.M070664.
623 Poehler, A. M., Xiang, W., Spitzer, P., May, V. E., Meixner, H., Rockenstein, E., Chutna, O.,
624 Outeiro, T. F., Winkler, J., Masliah, E. & Klucken, J. 2014. Autophagy modulates
625 SNCA/alpha-synuclein release, thereby generating a hostile microenvironment.
626 *Autophagy,* 10**,** 2171-92. DOI: https://doi.org/10.4161/auto.36436.
627 Raposo, G. & Stoorvogel, W. 2013. Extracellular vesicles: exosomes, microvesicles, and
628 friends. *J Cell Biol,* 200**,** 373-83. DOI: https://doi.org/10.1083/jcb.201211138.
629 Schneider, C. A., Rasband, W. S. & Eliceiri, K. W. 2012. NIH Image to ImageJ: 25 years of
630 image analysis. *Nat Methods,* 9**,** 671-5. DOI:
631 https://doi.org/10.1038/nmeth.2089.
632 Tang, Y., Cai, Q. H., Wang, Y. J., Fan, S. H., Zhang, Z. F., Xiao, M. Q., Zhu, J. Y., Wu, D. M., Lu,
633 J. & Zheng, Y. L. 2017. Protective effect of autophagy on endoplasmic reticulum
634 stress induced apoptosis of alveolar epithelial cells in rat models of COPD. *Biosci*
635 *Rep,* 37. DOI: https://doi.org/10.1042/BSR20170803.
636 Teis, D., Saksena, S., Judson, B. L. & Emr, S. D. 2010. ESCRT-II coordinates the assembly of
637 ESCRT-III filaments for cargo sorting and multivesicular body vesicle formation.
638 *EMBO J,* 29**,** 871-83. DOI: https://doi.org/10.1038/emboj.2009.408.
639 Ternes, P., Franke, S., Zahringer, U., Sperling, P. & Heinz, E. 2002. Identification and
640 characterization of a sphingolipid delta 4-desaturase family. *J Biol Chem,* 277**,**
641 25512-8. DOI: https://doi.org/10.1074/jbc.M202947200.
642 Thery, C., Boussac, M., Veron, P., Ricciardi-Castagnoli, P., Raposo, G., Garin, J. & Amigorena,
643 S. 2001. Proteomic analysis of dendritic cell-derived exosomes: a secreted
644 subcellular compartment distinct from apoptotic vesicles. *J Immunol,* 166**,** 7309-
645 18. DOI: https://doi.org/10.4049/jimmunol.166.12.7309.
646 Thery, C., Witwer, K. W., Aikawa, E., Alcaraz, M. J., Anderson, J. D., Andriantsitohaina, R.,
647 Antoniou, A., Arab, T., Archer, F., Atkin-Smith, G. K., Ayre, D. C., Bach, J. M.,
648 Bachurski, D., Baharvand, H., Balaj, L., Baldacchino, S., Bauer, N. N., Baxter, A. A.,

Bebawy, M., Beckham, C., Bedina Zavec, A., Benmoussa, A., Berardi, A. C., Bergese, P., Bielska, E., Blenkiron, C., Bobis-Wozowicz, S., Boilard, E., Boireau, W., Bongiovanni, A., Borras, F. E., Bosch, S., Boulanger, C. M., Breakefield, X., Breglio, A. M., Brennan, M. A., Brigstock, D. R., Brisson, A., Broekman, M. L., Bromberg, J. F., Bryl-Gorecka, P., Buch, S., Buck, A. H., Burger, D., Busatto, S., Buschmann, D., Bussolati, B., Buzas, E. I., Byrd, J. B., Camussi, G., Carter, D. R., Caruso, S., Chamley, L. W., Chang, Y. T., Chen, C., Chen, S., Cheng, L., Chin, A. R., Clayton, A., Clerici, S. P., Cocks, A., Cocucci, E., Coffey, R. J., Cordeiro-Da-Silva, A., Couch, Y., Coumans, F. A., Coyle, B., Crescitelli, R., Criado, M. F., D'souza-Schorey, C., Das, S., Datta Chaudhuri, A., De Candia, P., De Santana, E. F., De Wever, O., Del Portillo, H. A., Demaret, T., Deville, S., Devitt, A., Dhondt, B., Di Vizio, D., Dieterich, L. C., Dolo, V., Dominguez Rubio, A. P., Dominici, M., Dourado, M. R., Driedonks, T. A., Duarte, F. V., Duncan, H. M., Eichenberger, R. M., Ekstrom, K., El Andaloussi, S., Elie-Caille, C., Erdbrugger, U., Falcon-Perez, J. M., Fatima, F., Fish, J. E., Flores-Bellver, M., Forsonits, A., Frelet-Barrand, A., et al. 2018. Minimal information for studies of extracellular vesicles 2018 (MISEV2018): a position statement of the International Society for Extracellular Vesicles and update of the MISEV2014 guidelines. *J Extracell Vesicles,* 7**,** 1535750. DOI: https://doi.org/10.1080/20013078.2018.1535750.

Trajkovic, K., Hsu, C., Chiantia, S., Rajendran, L., Wenzel, D., Wieland, F., Schwille, P., Brugger, B. & Simons, M. 2008. Ceramide triggers budding of exosome vesicles into multivesicular endosomes. *Science,* 319**,** 1244-7. DOI: https://doi.org/10.1126/science.1153124.

Vaccari, T. & Bilder, D. 2005. The Drosophila tumor suppressor vps25 prevents nonautonomous overproliferation by regulating notch trafficking. *Dev Cell,* 9**,** 687-98. DOI: https://doi.org/10.1016/j.devcel.2005.09.019.

Vallabhaneni, K. C., Penfornis, P., Dhule, S., Guillonneau, F., Adams, K. V., Mo, Y. Y., Xu, R., Liu, Y., Watabe, K., Vemuri, M. C. & Pochampally, R. 2015. Extracellular vesicles from bone marrow mesenchymal stem/stromal cells transport tumor regulatory microRNA, proteins, and metabolites. *Oncotarget,* 6**,** 4953-67. DOI: https://doi.org/10.18632/oncotarget.3211.

Villarroya-Beltri, C., Baixauli, F., Mittelbrunn, M., Fernandez-Delgado, I., Torralba, D., Moreno-Gonzalo, O., Baldanta, S., Enrich, C., Guerra, S. & Sanchez-Madrid, F. 2016. ISGylation controls exosome secretion by promoting lysosomal degradation of MVB proteins. *Nat Commun,* 7**,** 13588. DOI: https://doi.org/10.1038/ncomms13588.

Wollert, T. & Hurley, J. H. 2010. Molecular mechanism of multivesicular body biogenesis by ESCRT complexes. *Nature,* 464**,** 864-9. DOI: https://doi.org/10.1038/nature08849.

Figures

Figure 1

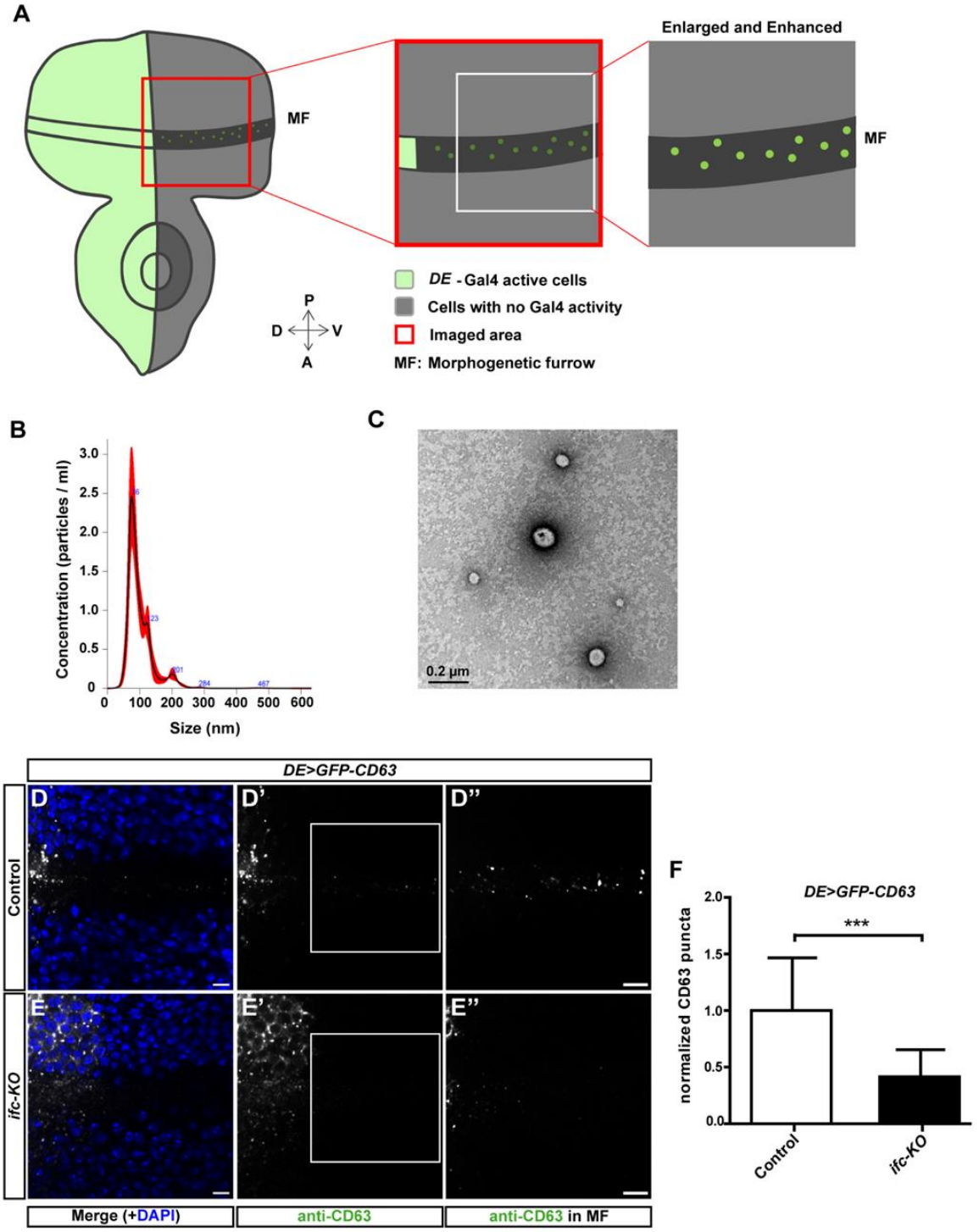

695 **Figure 1. Knocking out *ifc* reduces the number of released exosomes *in***
696 ***vivo*. (A)** A schematic illustration of the system for observing the release of
697 exosomes. *Dorsal-Eye Gal4* (*DE-Gal4*) drives the expression of *UAS-GFP-CD63*
698 in the dorsal half of the eye imaginal disc (green). The secreted exosomes that
699 move towards the ventral side alone the morphogenetic furrow (MF) into the
700 ventral side where images were taken (red box). The intensity and contrast were
701 linearly enhanced for the quantification of fluorescent puncta in the MF within the
702 region of interest (ROI, white box). **(B)** The representative size distribution of
703 exosomes collected from approximately 50 eye imaginal discs determined by
704 nanoparticle tracking analysis using Nanosight NS300. **(C)** Representative image
705 showing the morphology of exosomes by transmission electron microscopy. **(D-**
706 **E)** Representative confocal images of *Drosophila* eye imaginal discs with dorsally
707 expressed GFP-CD63 in FRT control (B-B”) and *ifc-KO* (C-C”) showing signals
708 merged with DAPI in blue (B,C), GFP-CD63 detected by anti-CD63 staining in
709 white (B’,C’), and enlarged images of the ROIs with linearly enhanced brightness
710 and contrast to show the GFP-CD63 puncta in the MF (B”,C”). Scale bars: 10
711 μm. **(F)** Quantification of GFP-CD63 puncta. Bar charts show mean ± SEM of at
712 least three independent experiments. *** $p < 0.001$ (Student’s *t*-test).
713

714 **Figure 2**

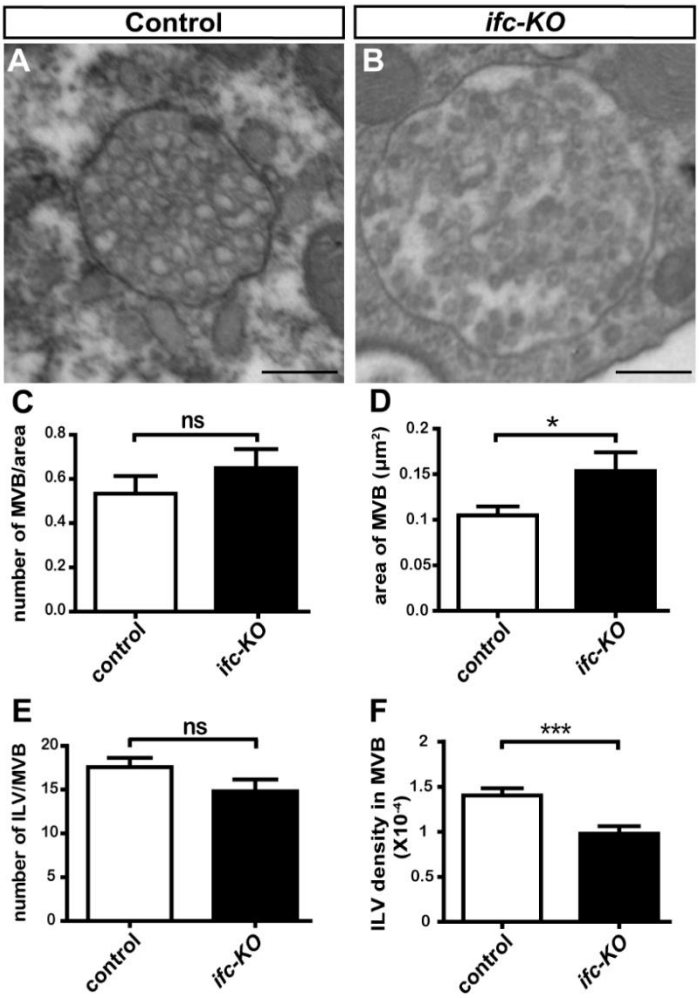

715

716 **Figure 2. Knocking-out *ifc* reduces the density of intraluminal vesicles**
717 **(ILVs) inside of multivesicular endosomes (MVEs). (A and B)** Representative
718 transmission electron microscopy (TEM) images of the wild-type control (A) and
719 *ifc-KO* photoreceptors (B) after 3 days of light stimulation. Scale bars: 250 nm.
720 **(C-F)** Quantification of TEM images including the number of MVEs per field (C),
721 the area of MVEs (D), the number of ILVs per MVE (E), and the number of ILVs
722 per unit area of MVEs (F). Bar charts show mean ± SEM of at least three
723 independent experiments. *** $p < 0.001$; * $p < 0.05$; ns: Not significant (Student's
724 *t*-test).

725

726 **Figure 3**

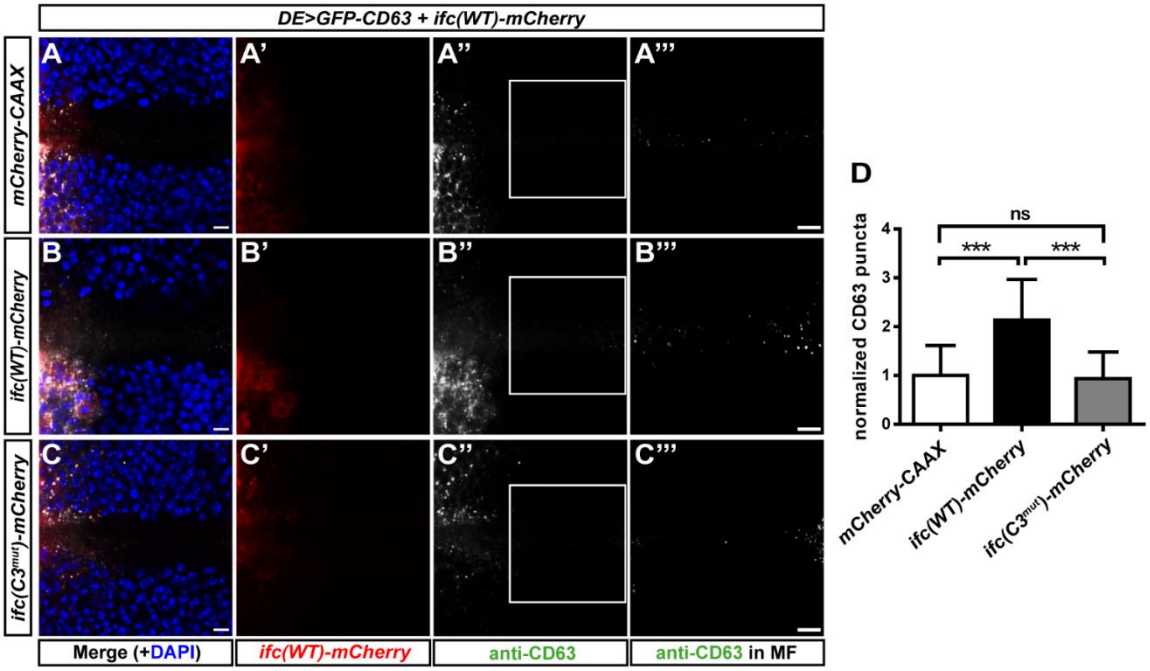

727

728 **Figure 3. Enhancing *ifc* activity increases the number of exosomes. (A-B)**
729 Representative confocal images of *Drosophila* eye imaginal discs with dorsally
730 expressed *GFP-CD63* with the UAS control *mCherry-CAAX* (D-D'''), *ifc(WT)-*
731 *mCherry* (E-E'''), or *ifc(C3^{mut})-mCherry* (F-F''') showing merged images with DAPI
732 in blue (D,E,F), mCherry fluorescence in red (D',E',F'), anti-CD63 staining in
733 white (D",E",F"), and enlarged images of the ROI (white box) with linearly
734 enhanced brightness and contrast to reveal GFP-CD63 puncta in the MF
735 (D''',E''',F'''). Scale bars: 10 μm. **(G)** Quantification of GFP-CD63 puncta. Bar
736 charts show mean ± SEM of at least three independent experiments. *** $p <$
737 0.001; ns: Not significant (Student's *t*-test).

738

739 **Figure 4**

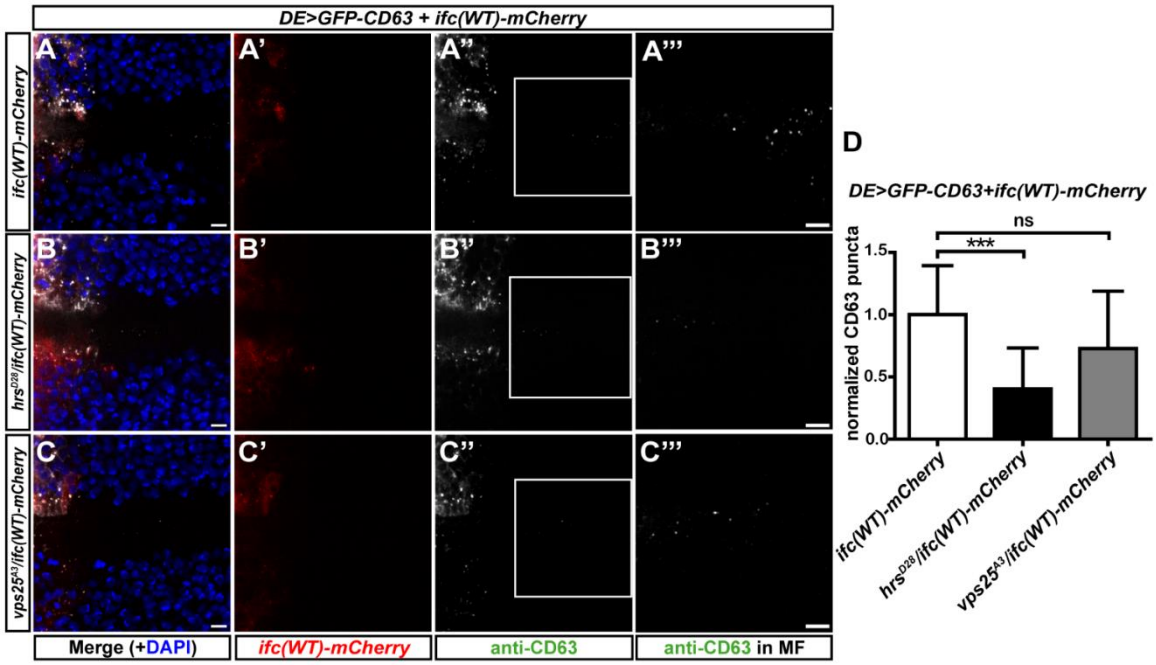

740

741 **Figure 4. Ifc genetically interacts with ESCRT genes to regulate exosome**
742 **production. (A-C)** Confocal images of *Drosophila* eye imaginal discs with
743 dorsally expressed *GFP-CD63* and *ifc(WT)-mCherry* in the control (A), $hrs^{D28/+}$
744 (B), and $vps25^{A3/+}$ (C) showing merged images with DAPI in blue (A,B,C),
745 mCherry fluorescence in red (A',B',C'), anti-CD63 staining in white (A",B",C"), and
746 enlarged images of the ROI (white box) with linearly enhanced brightness and
747 contrast to reveal GFP-CD63 puncta in the MF in the ROIs (A'",B'",C'"). Scale
748 bars: 10 μm. **(D)** Quantification of GFP-CD63 puncta. Bar charts show mean ±
749 SEM of at least three independent experiments. *** $p < 0.001$; ns: Not significant
750 (one-way ANOVA).

751

752 **Figure 5**

A

DEGS1	dhCer	ILV (%)	N
-	-	0%	10
+	-	0%	10
-	dhCer	0%	20
+	dhCer	31.81%	22

F

DEGS1	Fenretinide	ILV (%)	N
-	EtOH	0%	10
+	EtOH	36.36%	11
-	+	0%	9
+	+	0%	9

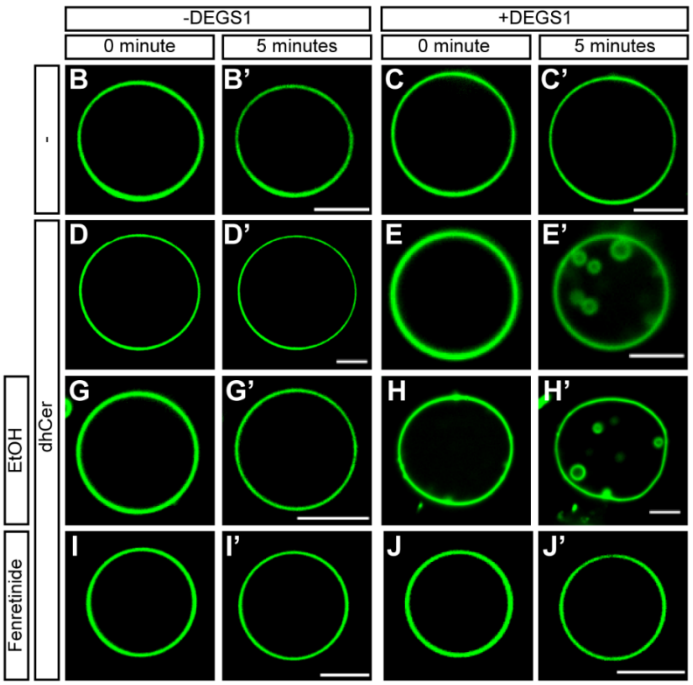

753

754 **Figure 5. DEGS1 drives the formation of ILVs in the giant unilamellar**
755 **vesicles (GUVs) *in vitro*. (A)** Table summary of the percentages of GUVs that
756 formed ILVs within 5 min with or without dhCer and recombinant DEGS1 protein.
757 **(B-E)** Representative images of GUVs in (A). **(F)** Table summary of the
758 percentages of GUVs that showed ILV formation within 5 min with and without
759 DEGS1 protein in the presence of ethanol (EtOH) solvent or 0.2 μM fenretinide, a
760 DEGS1 inhibitor. **(G-J)** Representative images of GUVs in (F). Scale bar: 5 μm.
761

762 **Figure 6**

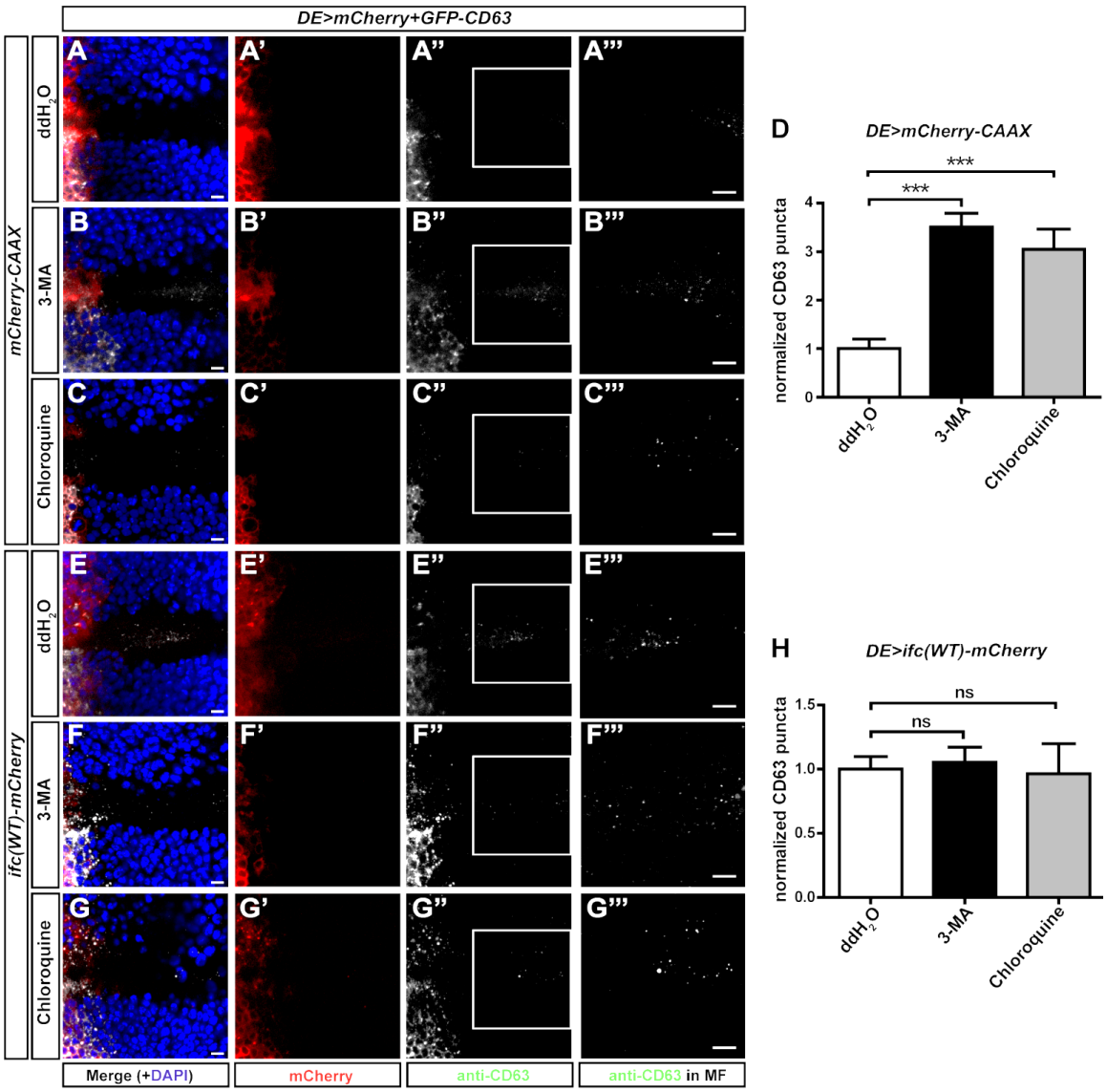

763

764 **Figure 6. Ifc promotes exosome secretion by blocking autophagy-mediated**
765 **degradation of MVEs. (A-C)** Representative confocal images of *Drosophila* eye
766 imaginal discs with dorsally expressed *GFP-CD63* treated with ddH_2O (A-A'''), 3-
767 methyladenine (3-MA, B-B'''), and chloroquine (C-C''') showing merged images
768 with DAPI in blue (A,B,C), mCherry in red (A',B',C'), anti-CD63 staining in white
769 (A",B",C"), and enlarged images of the ROI (white box) with linearly enhanced
770 brightness and contrast to show GFP-CD63 puncta in the MF (A''',B''',C'''). **(D)**
771 Quantification of GFP-CD63 puncta. **(E-G)** Representative confocal images of

772 *Drosophila* eye imaginal discs with dorsally expressed GFP-CD63 and *ifc(WT)-*
773 *mCherry* treated with ddH_2O (E-E'''), 3-methyladenine (3-MA, F-F'''), and
774 chloroquine (G-G''') showing merged images with DAPI in blue (E,F,G), Ifc(WT)-
775 mCherry in red (E',F',G'), anti-CD63 staining in white (E",F",G"), and enlarged
776 images of the ROI with linearly enhanced brightness and contrast to show GFP-
777 CD63 puncta in the MF (E''',F''',G'''). **(H)** Quantification of GFP-CD63 puncta.
778 Scale bars: 10 μm. Bar charts show mean ± SEM of at least three independent
779 experiments. *** $p < 0.001$; ns: Not significant (Student's *t*-test).
780

781 **Supplemental Figure 1**

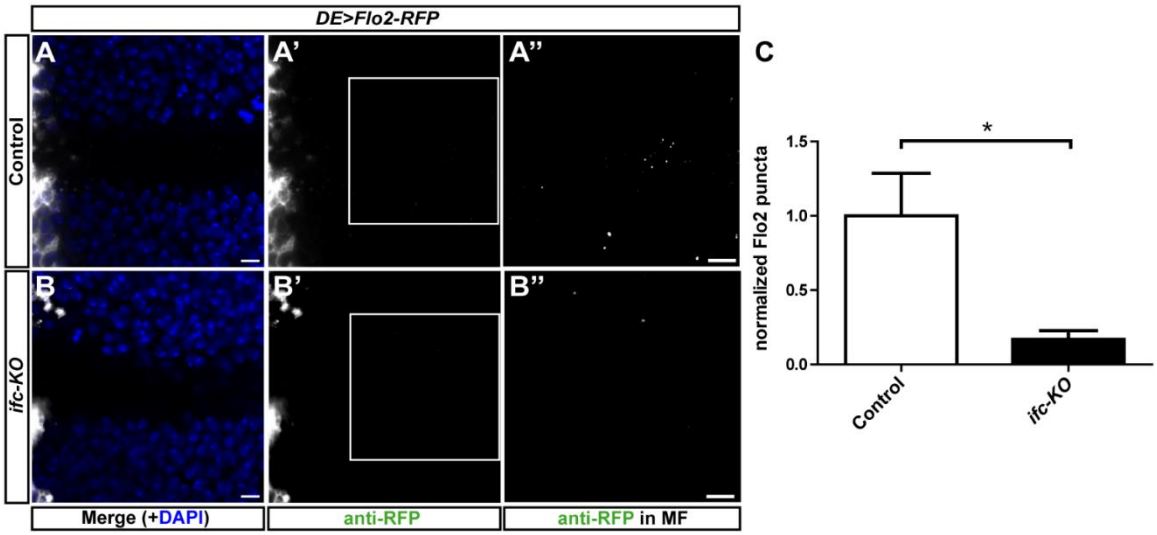

782

783 **Figure S1. Knocking out *ifc* reduces the number of Flo2-labelled exosomes.**
784 **(A-B)** Representative confocal images of *Drosophila* eye imaginal discs
785 expressing Flo2-RFP in the dorsal compartment in the FRT control (A-A'') and *ifc-*
786 *KO* eyes (B-B'') showing merged images with DAPI in blue (A,B), Flo2-RPF
787 signal enhanced by anti-RFP staining pseudocolored in white (A',B') and
788 enlarged and linearly enhanced images of the ROI (white box) to reveal Flo2-
789 RFP puncta in the MF (A"-B"). Scale bars: 10 µm. **(C)** Quantification of Flo2-RFP
790 puncta. Bar charts show mean ± SEM of at least three independent experiments.
791 * $p < 0.05$ (Student's *t*-test).
792

793 **Supplemental Figure 2**

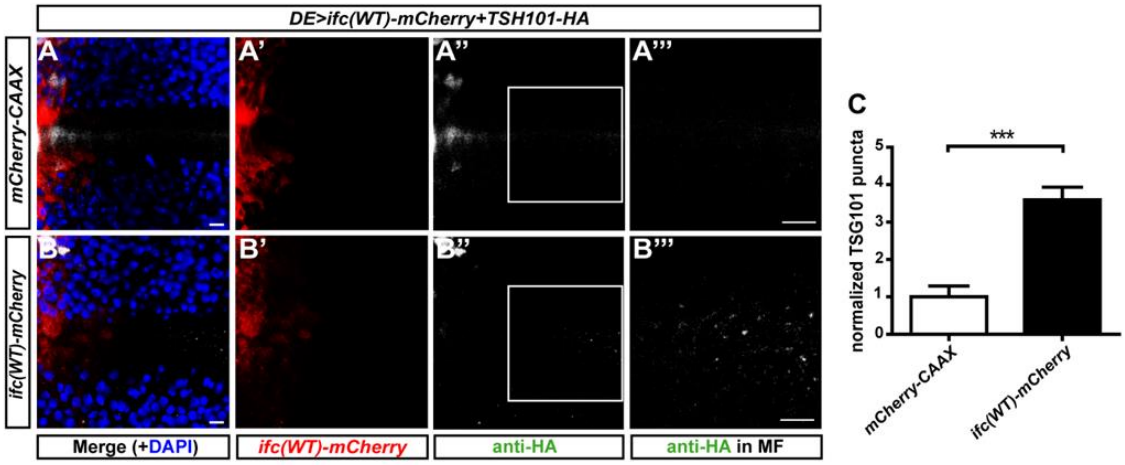

794

795 **Figure S2. Enhancing *ifc* activity increases the release of TSG101-HA-**
796 **labelled exosomes.** Representative confocal images of *Drosophila* eye imaginal
797 discs dorsally expressed *TSG101-HA* with UAS *mCherry-CAAX* (control, A-A'''')
798 or *ifc(WT)-mCherry* (B-B'''') showing merged images with DAPI in blue (A,B),
799 mCherry fluorescence in red (A',B'), anti-HA staining in white (A'',B''), and
800 enlarged images of the ROI (white box) with linearly enhanced brightness and
801 contrast to reveal TSG101-HA puncta in the MF (A'''',B''''). Scale bars: 10 µm. **(C)**
802 Quantification of TSG101-HA puncta. Bar charts show mean ± SEM of at least
803 three independent experiments. *** $p < 0.001$; ns: Not significant (Student's *t*-
804 test).

805

806 **Supplemental Figure 3**

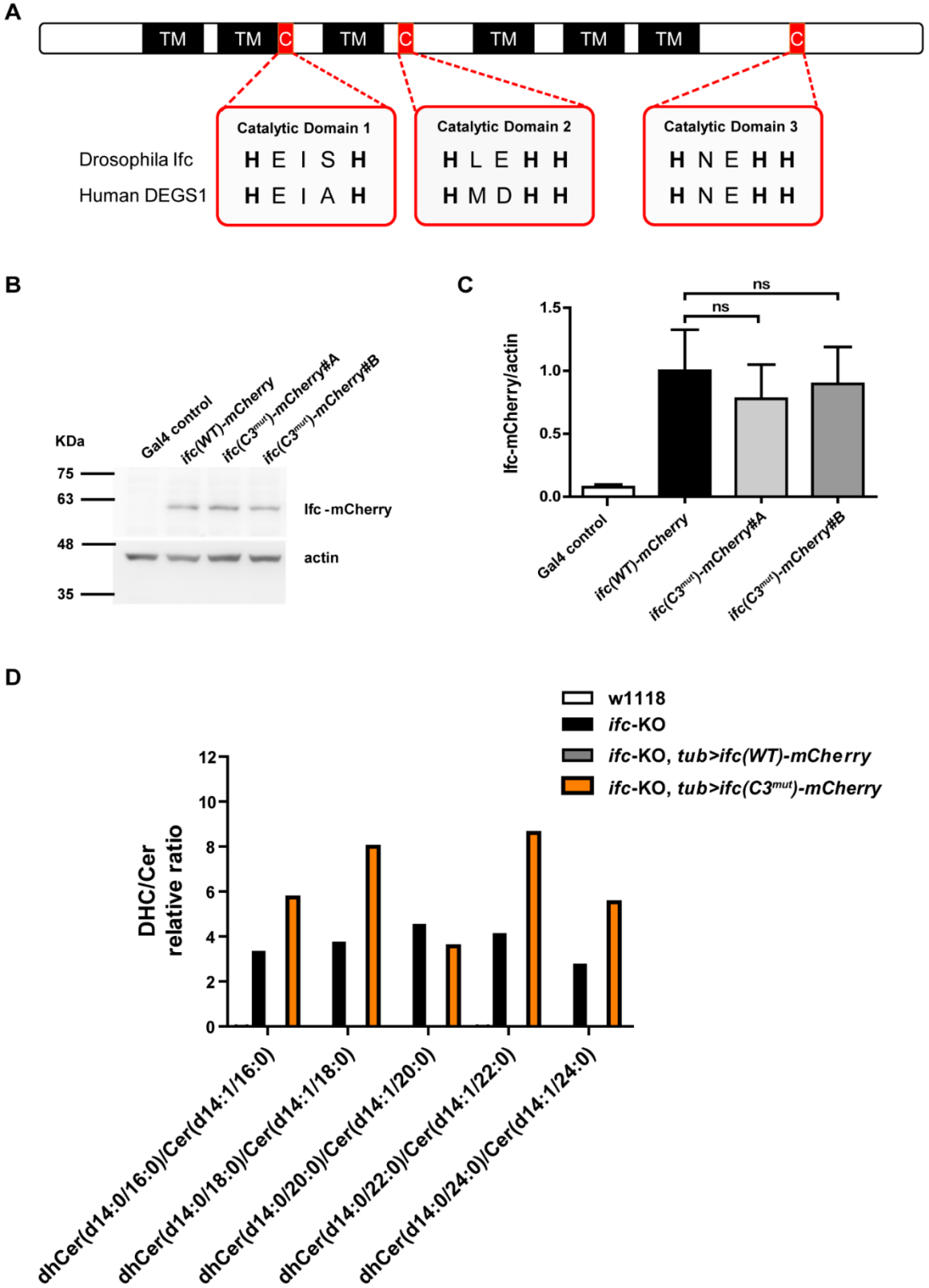

807

808 **Figure S3. The construction and characterization of transgenically**
809 **expressed *ifc(C3^{mut})-mCherry*. (A)** A schematic illustration of the histidine-rich
810 regions that are key catalytic domains of dihydroceramide desaturases. The
811 amino acid sequences of the catalytic domains are highly conserved between
812 *Drosophila* Ifc and Human DEGS1. TM: predicted transmembrane domains; C:
813 histidine-rich catalytic domains. **(B)** Western blot analysis of Ifc-mCherry proteins
814 expressed in flies under *nSyb-Gal4*. Actin was used as the loading control. **(C)**
815 Quantification of the protein levels of mCherry-tagged *ifc* transgenes relative to
816 actin. Normalized to *ifc(WT)-mCherry*. ns: Not significant (Student's *t*-test). **(D)**
817 The dhCer-to-Cer ratio of *w1118* control; *ifc-KO* alone; *ifc-KO*,*tub>ifc(WT)-*
818 *mCherry*; and *ifc-KO,tub>ifc(C3^{mut})-mCherry* measured by HPLC-MS/MS.
819

820 **Supplemental Figure 4**

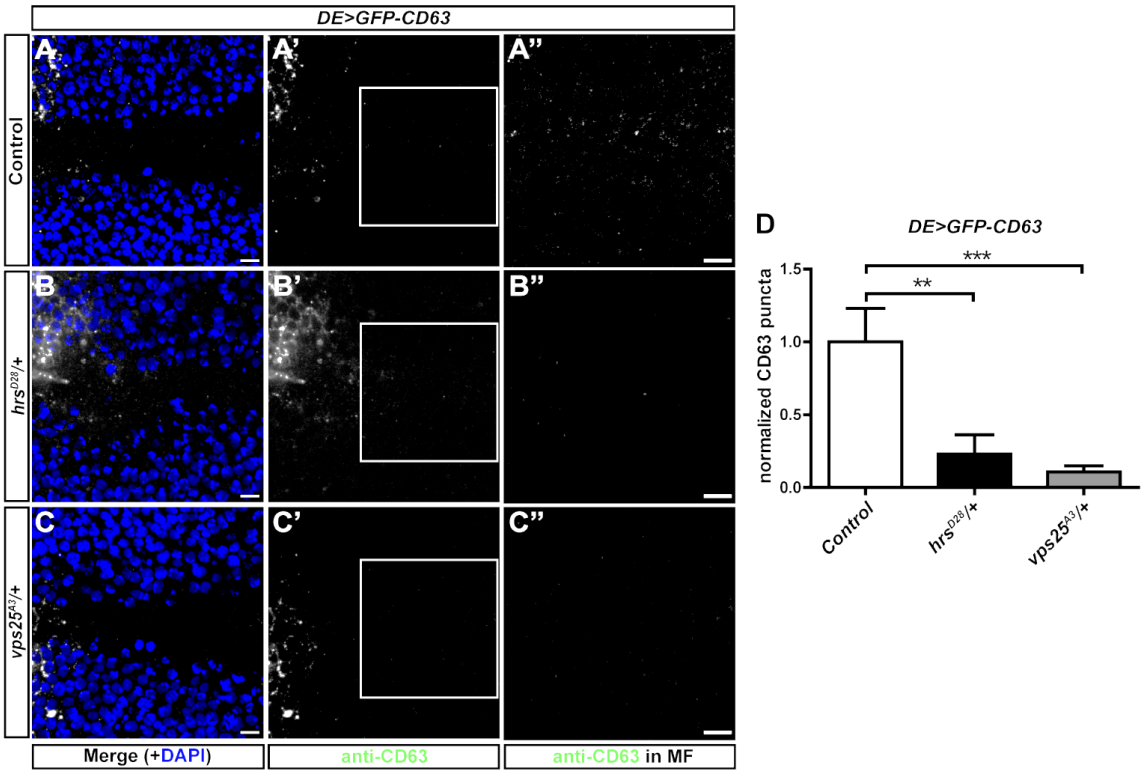

821

822 **Figure S4. Heterozygous mutations in the ESCRT genes *hrs* and *vps25***
823 **reduce the number of exosomes. (A-C)** Confocal images of *Drosophila* eye
824 imaginal discs with dorsally expressed *GFP-CD63* in the wile-type control (A),
825 $hrs^{D28/+}$ (B), and $vps25^{A3/+}$ (C) showing merged images with DAPI in blue (A,B,C),
826 anti-CD63 staining in white (A',B',C'), and enlarged images of the ROI (white box)
827 with linearly enhanced brightness and contrast to reveal GFP-CD63 puncta in the
828 MF in the ROIs (A",B",C"). Scale bars: 10 µm. **(D)** Quantification of GFP-CD63
829 puncta. Bar charts show mean ± SEM of at least three independent experiments.
830 *** $p < 0.001$; ** $p < 0.01$ (one-way ANOVA).
831

832 **Supplemental video 1**

833 Live imaging by spinning disc confocal microscopy of GFP-CD63 puncta
834 produced by eye imaginal disc over-expressing Ifc(WT)-mCherry *ex vivo*.

835

836 **Supplemental video 2**

837 Live imaging by spinning disc confocal microscopy of GFP-CD63 puncta
838 produced by mCherry-CAAX control eye imaginal disc.

839

840 **Supplemental video 3**

841 Light-sheet microscopy of GFP-CD63 puncta produced by eye imaginal disc
842 over-expressing Ifc(WT)-mCherry.

843

844 **Supplemental video 4**

845 Light-sheet microscopy of GFP-CD63 puncta produced by the mCherry-CAAX
846 control imaginal disc.